Slag Mass Accumulation in Spinning Solid Rocket Motors

V. E. Haloulakos*
McDonnell Douglas Space Systems Company, Huntington Beach, California 92647

A series of specific solid propellant rocket motors are evaluated and their slag mass accumulation is computed when operating in strong acceleration environments. It is shown that the configuration of the propellant burning surface during the last 10 s of burning has a very strong effect on slag formation. Motors with front-end burning grains at burnout have maximum slag retention potential, whereas motors with the grain burning inside potential slag pockets (e.g., the buried nozzle cavities) do not accumulate any slag. The effects of the internal flowfield are significant because they are the direct result of the grain configuration. It is concluded that if slag is a problem, selective grain design will tend to minimize it or to eliminate it completely.

Nomenclature

A = area
a = acceleration
a_{ys} = side acceleration caused by the transverse coning motion
C_D = drag coefficient
D = drag force
d = particle diameter
e_d = unit vector in the direction of the drag
F = thrust force
m = mass
Re = Reynolds number
t = time
V = velocity
X, Y = position coordinates
μ = gas viscosity
ρ = density
ω = vehicle spin rate

Subscripts

b = body
g = gas
p = particle
r = relative
v = vehicle
x,y = x or y direction

Introduction

A GYROSCOPIC precession phenomenon termed "coning" has been encountered in the flights of spin-stabilized vehicles operating either out of the Space Shuttle or the upper stages of ground-launched expendable launch vehicles (ELV) powered by solid propellant rocket motors. Because of envelope limitations, these rocket motors employ "buried nozzles," i.e., the exhaust nozzle extends far into the rocket motor case, as shown in Fig. 1. This results in a large cavity within the motor case where small metal oxide particles, a direct result of the combustion process in the high-performance metallized solid propellant, may be trapped instead of being expelled out of the nozzle. This mass accumulation is termed slag, and it has been identified as a possible cause for the observed gyroscopic instabilities. The slag mass also has an effect on the rocket motor performance since it is not expelled out of the nozzle to produce thrust and it must also be accelerated as additional inert mass during the flight.

The primary goal of this paper is to treat the subject of the slag formation and compute the quantities of slag in solid propellant rocket motors currently in use under typical flight conditions of both axial and radial (spin) accelerations. A secondary goal is to discuss and assess the associated performance variations caused by the formation of slag.

The general approach to the problem used here is that of two-phase flow, which is similar to that used by Boraas.[1] Whereas Boraas' treatment was basically concerned with the solid propellant rocket boosters used in the Space Shuttle, this paper treats a variety of motors that are smaller in size and are spinning for stabilization. In the Space Shuttle solid rocket motors (SS-SRM), the problem is that of long residence time of the solid aluminum oxide (Al_2O_3) particles within the motor case; in the smaller motors the problem is more a combination of both axial and radial accelerations. These will cause the Al_2O_3 particle paths to deviate from the gas flow streamlines and be deposited in the stagnant flow cavities in the buried nozzle region. Thus, near the end of its powered flight, the spacecraft may have substantial quantities of added inert mass that must be accelerated and, because of its molten nature, this mass may be swirled around, thus causing vehicle mass asymmetry and gyroscopic instability.

Mathematical Model

The basic problem addressed here is that of particle motion through viscous media subject to the influence of both drag and body forces. The drag forces are caused by the flowing gases and the body forces are the result of the vehicle spin and axial acceleration. The basic model is composed of two parts: the gas flowfield within the motor case and the solid particle motion in the gas.

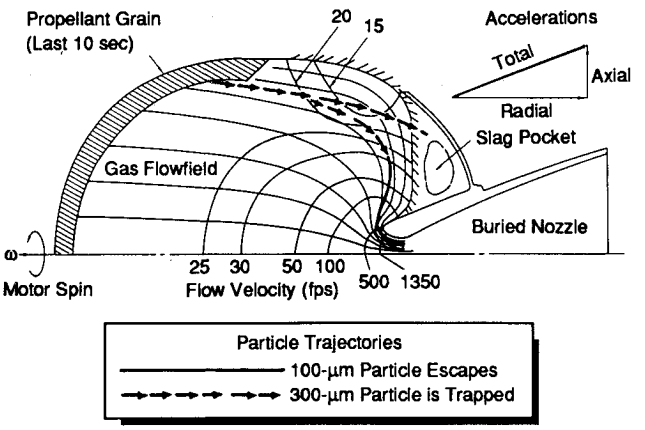

Fig. 1 Slag formation mechanism—particle entrapment schematic.

Received May 8, 1989; revision received Dec. 15, 1989.

*Space Propulsion Specialist, Design Technology Center. Associate Fellow AIAA.

Gas Flowfield

The gas flowfield was calculated by the potential flow program TAPS (Transition Analysis Program System), described in Refs. 2 and 3. The basic input to the program is the motor internal geometry, including the dividing streamline at the buried nozzle cavity and the throat region, and a series of sources simulating the gas flow emanating from the propellant burning surface. The program output is a description of the flowfield in terms of its velocity components V_{gx} and V_{gy} in the x and y directions, respectively, for each specified point (x,y).

Particle Motion Model

A particle starts out with a specific set of initial conditions in terms of its point of origin and its initial velocity vector. It is subjected to the drag forces by the viscous fluid and the body forces caused by the vehicle spin and the forward acceleration.

The equations of motion for the solid particles are the following:

Body forces:

$$\mathbf{a}_{bp} = \mathbf{i}a_{bpx} + \mathbf{j}a_{bpy} \tag{1}$$

$$a_{bpy} = \omega^2 y + a_{ys} \tag{2}$$

$$a_{bpx} = F_{bx}/m_p \tag{3}$$

$$\mathbf{F}_b = m_p \mathbf{a}_{bp} \tag{4}$$

Drag forces:

$$\mathbf{D} = C_D 1/2 \rho_g A_p V_r^2 \mathbf{e}_d \tag{5}$$

The relative velocity and the drag components are as follows:

$$V_{rx} = V_{gx} - V_{px} \tag{6}$$

$$V_{ry} = V_{gy} - V_{py} \tag{7}$$

$$V_r^2 = V_{rx}^2 + V_{ry}^2 \tag{8}$$

The particle area is given by

$$Ap = (\pi d_p^2)/4 \tag{9}$$

and the drag coefficient is

$$C_D = 27/Re^{0.84}\ 0 < Re < 80 = 0.271\ Re^{0.217}\ 80 \leq Re < 10^4 = 2.0\ Re \geq 10^4 \tag{10}$$

where

$$Re = [d_p(V_g - V_p)\rho g] / \mu_g \tag{11}$$

The drag force components are

$$D_x = D(V_{rx}/V_r) \tag{12}$$

$$D_y = D(V_{ry}/V_r) \tag{13}$$

The accelerations caused by the gas forces are

$$a_{gpx} = D_x/m_p \tag{14}$$

$$a_{gpy} = D_y/m_p \tag{15}$$

The combined gas and body accelerations are then integrated to calculate the changes in the particle velocities and positions as follows:

$$(a_{px})_i = (a_{bpx})_i + (a_{gpx})_i \tag{16}$$

$$(a_{py})_i = (a_{bpy})_i + (a_{gpy})_i \tag{17}$$

$$(V_{px})_i = (V_{bpx})_{i-1} + (a_{px})_i \Delta t \tag{18}$$

$$(V_{py})_i = (V_{bpy})_{i-1} + (a_{py})_i \Delta t \tag{19}$$

$$(\Delta X_p)_i = (V_{px})_i \Delta t \tag{20}$$

$$(\Delta Y_p)_i = (V_{py})_i \Delta t \tag{21}$$

$$(X_p)_i = (X_p)_{i-1} + (\Delta X_p)_i \tag{22}$$

$$(Y_p)_i = (Y_p)_{i-1} + (\Delta Y_p)_i \tag{23}$$

A numerical stability criterion is built into the program that checks and holds the maximum particle displacement within a preset limit. This becomes necessary near the throat region where the high gas velocities cause very high accelerations. When this check is encountered, the program keeps reducing the magnitude of the time increment Δt until the stability criteria are met.

The program computes and plots the particle positions, thus giving a graphical output of the particle trajectories and a very

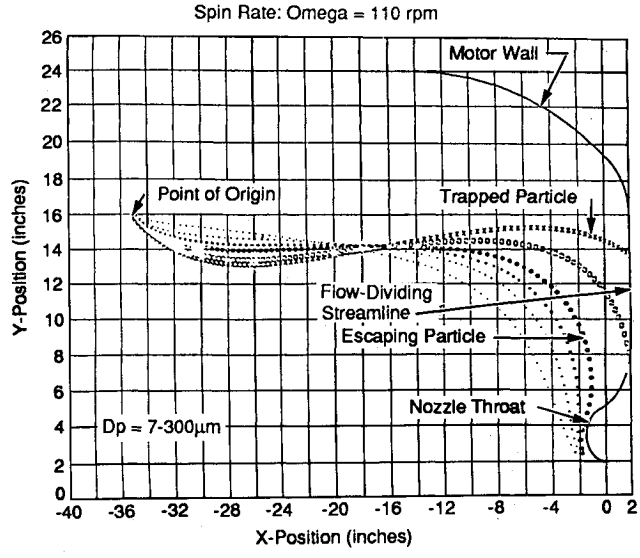

Fig. 2 Typical slag formation particle trajectory plots.

Table 1 Grain surface points considered

Point number	Coordinate axes; throat: $(x,y) = (0,0)$	
	x, in.	y, in.
1[a]	−42.0	0
2	−37.0	14.0
3	−35.0	16.0
4	−32.0	18.5
5	−28.0	20.5
6	−24.0	22.0
7	−22.0	22.0
8	−20.0	22.0
9	−18.0	22.0
10[b]	−12.0	20.5
11	−14.0	19.0
12	−16.0	17.5
13	−18.0	17.0
14	−20.0	17.0

[a]Points 1-9 represent 10 s and 1 s to burnout.
[b]Points 10-14 represent 30 s to burnout.

clear indication of the origin and final destination of each particle.

Model Validation

The computer program was used in evaluating the slag formation in specified solid propellant motors that could be checked with experimental data. The physical mechanism of slag accumulation is shown schematically in Fig. 1. The 100-μm particle is sufficiently small to follow the gas streamlines and, thus, escape from the nozzle. The 300-μm particle is heavier and the body forces cause its path to deviate from the streamlines and enter the cavity around the buried nozzle where it remains. This particle entrapment and accumulation is the formation of slag. The procedure was to define a solid propellant motor and compute the internal gas flow by the TAPS Neumann potential flow program.[2,3] The next step was to identify a set of particles and consider them as originating from different points along the burning surface. The computer code calculates the particle trajectory, which, when plotted, gives an immediate indication as to whether the particle will escape or not; the escape and/or entrapment criteria are shown in Fig. 2. For the purpose of preliminary evaluations, particle diameters from 7 to 300 μm were considered. Their points of origin were spread over the burning surface, representing burn times of 30, 10, and 1 s. Table 1 shows the coordinates of the particles' points of origin, the nozzle throat being the origin point of the coordinate axes.

Particle trajectories are plotted for each particular case studied for quick evaluation of the effects of grain geometry, axial and radial acceleration, etc. For example, Fig. 3 shows that all particles escape through the nozzle when there is neither spin (as in Fig. 2) nor axial acceleration present.

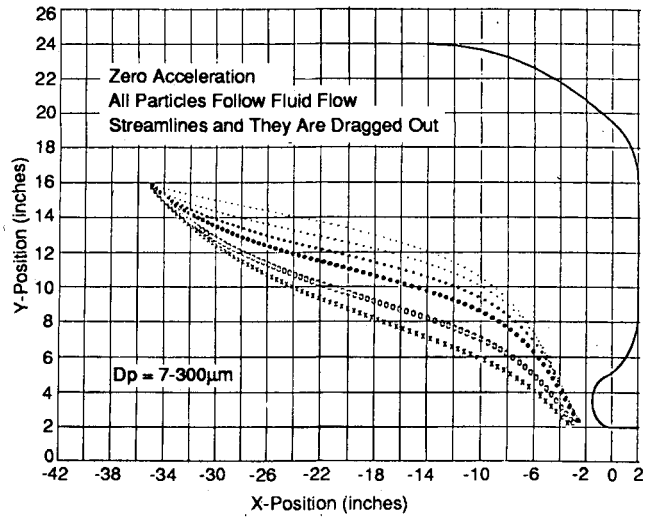

Fig. 3 Particle trajectories without acceleration.

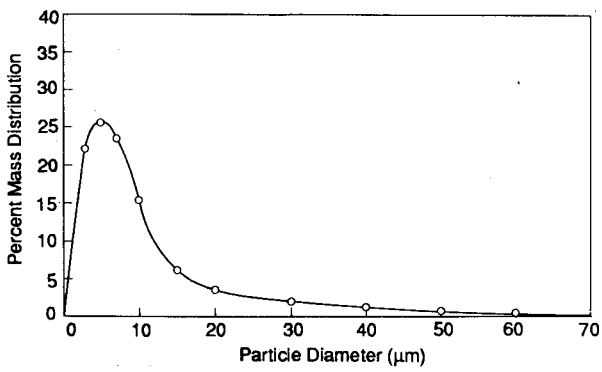

Fig. 4 Particle diameter distribution model.

The total mass of slag accumulated is calculated simply by counting the particles that remain inside and integrating them over the burning time. The problem that needed clarification was the particle sizes and their distribution in the combustion products. This was resolved by assuming various particle size distributions and, for each distribution, calculating the corresponding slag data and comparing them with available ex-

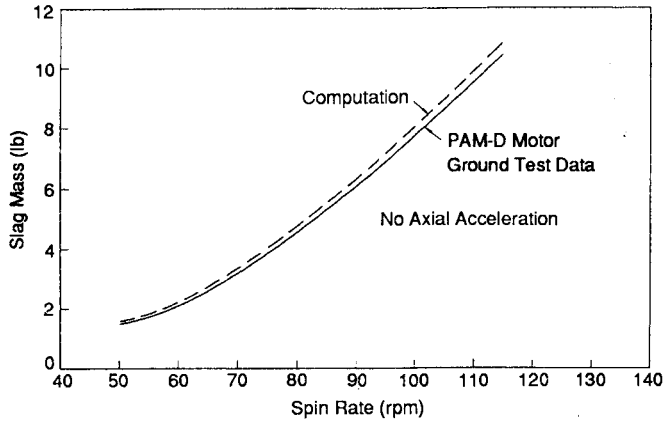

Fig. 5 Particle distribution model validation.

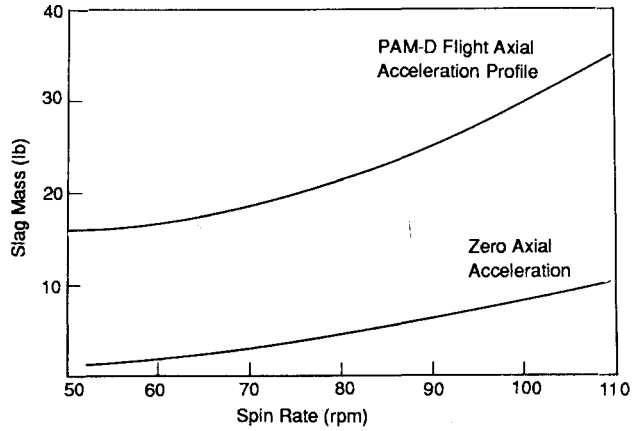

Fig. 6 PAM-D slag accumulation predictions.

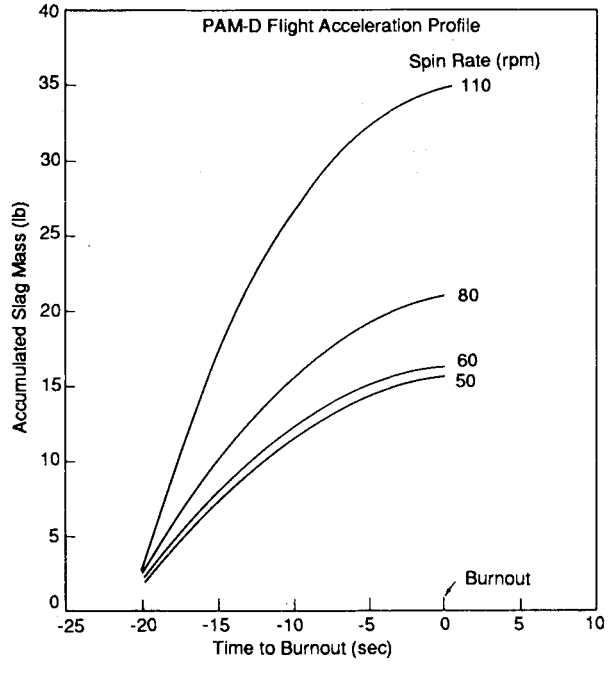

Fig. 7 Slag mass accumulation history.

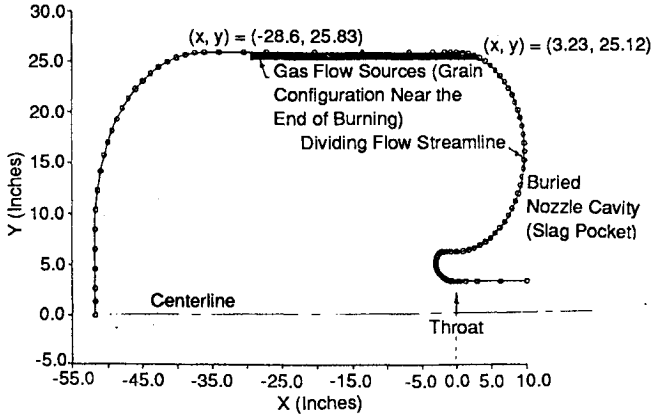

Fig. 8 Computer modeling of the PAM-A motor case and the internal source flow distribution.

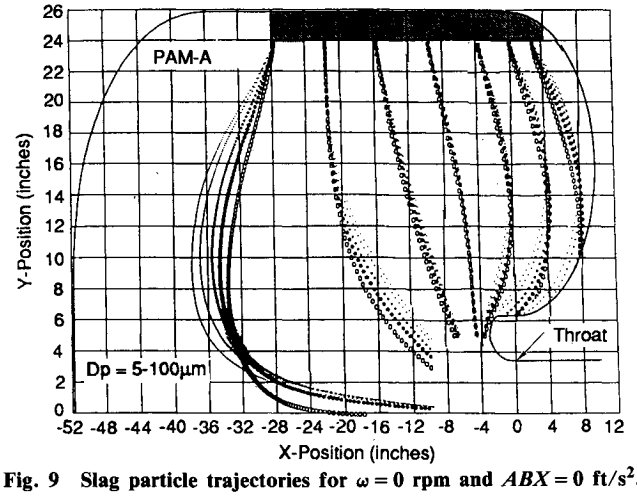

Fig. 9 Slag particle trajectories for $\omega = 0$ rpm and $ABX = 0$ ft/s^2.

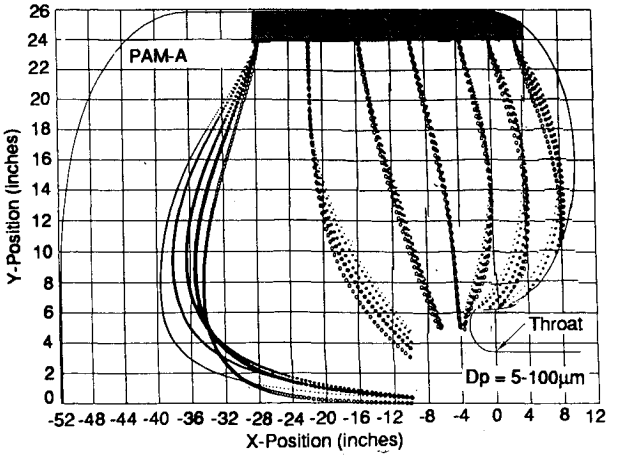

Fig. 10 Slag particle trajectories for $\omega = 40$ rpm and $ABX = 0$ ft/s^2.

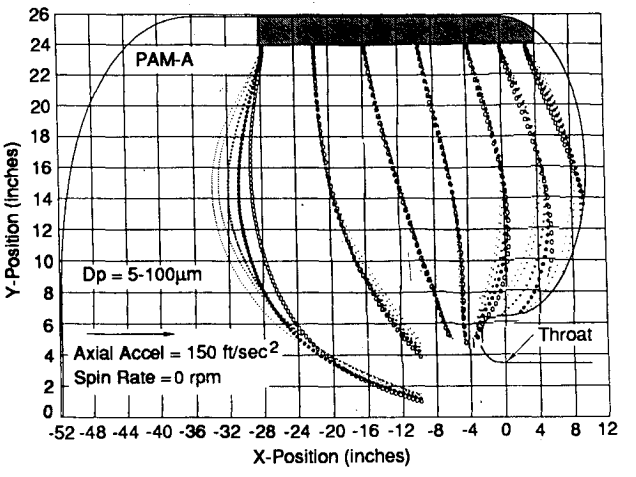

Fig. 11 Slag particle trajectories for $\omega = 0$ rpm and $ABX = 150$ ft/s^2.

perimental data from ground tests. Figure 4 represents a particle distribution that gives slag mass results that correlate with experimental data. Figure 5 shows the correlation between the computed and the experimental data.

Once the particle distribution model has been validated with experimental data, the computer code can calculate slag mass accumulated as a function of acceleration. A set of such data was generated for the PAM-D solid propellant motor as a function of spin rate for zero axial acceleration (i.e., the ground test data curve was duplicated) and also with axial accelerations representing a typical PAM-D flight acceleration profile (135–180 ft/s^2). The results are given in Fig. 6. The time accumulation history of slag for various spin rates is shown in Fig. 7. This indicates that slag accumulates during the last 20 or 30 s of the flight, a fact corroborated by experimental evidence.

Additional data and details covering the development and validation of the analysis model may be found in Ref. 4.

Evaluation of Specific Motors

These analyses and evaluation methods were applied to the PAM-A, TEM-364-4, and PAM-DII motors, and the accumulated slag mass was calculated. A motor similar to that used in the first stage of the United States Air Force (USAF) inertial upper stage (IUS) vehicle (i.e., the SRM-1) was also studied, but no slag mass calculations were made. Instead, this motor was used as the basis for evaluating the effects of large motor diameters on the internal flowfield and the propellant grain configurations.

PAM-A Motor

The motor case was described by a series of equations of circular arcs and straight lines that were computerized. A dividing flow streamline defining the boundary of the stagnant circulation region in the buried nozzle cavity was established and approximated by an appropriate equation. The computer plot resulting from these equations is shown in Fig. 8. The TAPS was again used to calculate the internal flowfield within the motor case.

A set of normalized flow sources, also shown in Fig. 8, was distributed to correspond with the propellant grain configuration near the end of burning. The configuration of the propellant grain burning surface determines the internal flowfield. Judicious placement of flow sources on the region corresponding to the surface adequately simulates the physics of the problem.

Slag particles (solid Al_2O_3) varying in diameter from 5 to 100 μm were placed at various intervals along the propellant burning surface. Their initial injection velocity into the flow was set at 10 ft/s normal to the burning surface. The computer code calculated and plotted the position trajectories of these particles by considering the balance of drag, spin, and axial forces. Motor spin rates ω up to 80 rpm and axial accelerations (ABX) up to 175 ft/s^2 were considered. Sample plots of the slag particle trajectories are shown in Figs. 9–12. Examination of these figures indicate that most of the slag particles escape through the nozzle with the exception of a small quantity from the aft portion of the propellant grain, especially at the higher spin and axial accelerations.

Assuming the Al_2O_3 particle size distribution in the combustion products as in Fig. 4, slag mass accumulation curves as a function of spin rate for 0 and 175 ft/s^2 axial acceleration were calculated. The data are shown in Fig. 13, where it should be noted that the zero axial-acceleration curve corre-

lates very well with the two ground test points at 40- and 70-rpm spin rates.

At high spin rates, the two curves come together indicating that the axial accelerations do not have a significant effect. Actually, a stagnant or circulation flow zone also exists at the head end of the motor (as indicated in the upper left corner of Fig. 8), and, at high spin rate, a portion of the Al_2O_3 particles originating near the front end of the grain curve into this zone and are trapped. Thus, under the influence of high spin rates alone, slag contributions come from both ends of the grain, whereas, when axial accelerations are added, only the aft end of the propellant grain contributes to the slag accumulation. It also turns out that under the combined effects of both high spin and high axial accelerations, if all of the Al_2O_3 particles from the contributing zone were trapped, a maximum of 20 lb of slag would be accumulated. Thus, the computed data shown here are in close agreement.

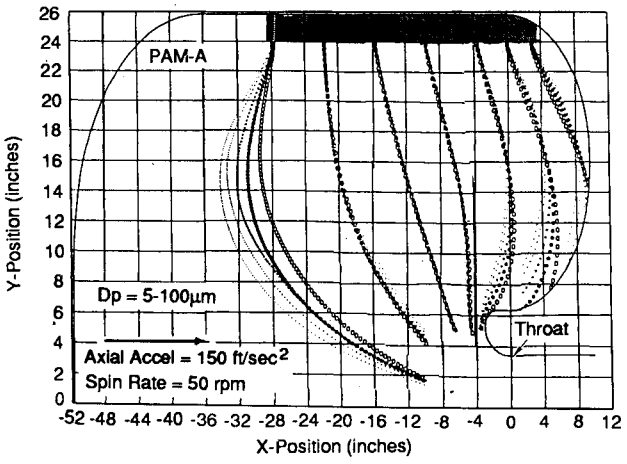

Fig. 12 Slag particle trajectories for $\omega = 50$ rpm and $ABX = 150$ ft/s^2.

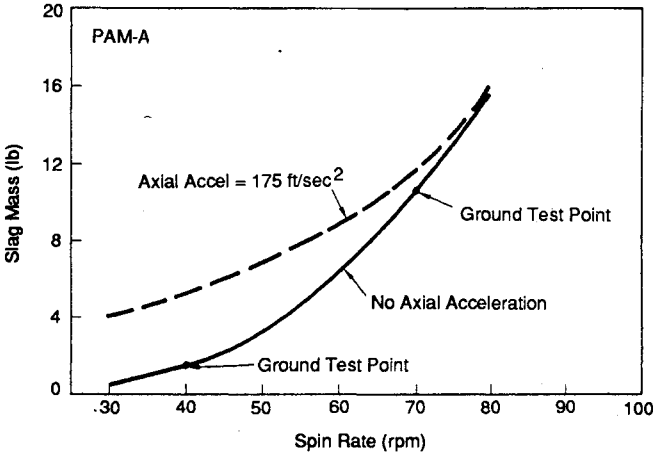

Fig. 13 PAM-A slag mass accumulation variation with spin rate.

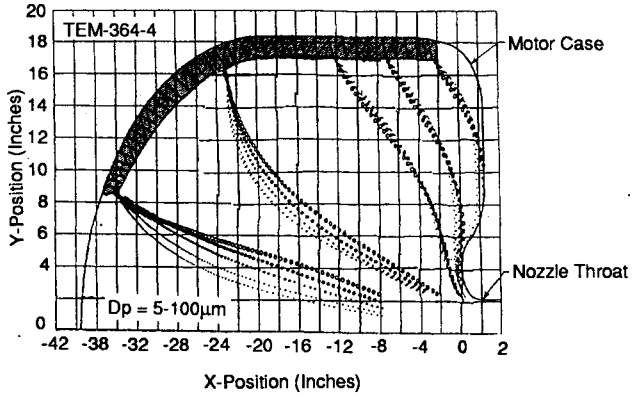

Fig. 14 TEM 364-4 slag particle trajectories for $\omega = 75$ rpm and $ABX = 210$ ft/s^2.

TEM-364-4 and PAM-DII Motors

The same analysis and evaluation methods were applied to the TEM-364-4 and the PAM-DII motors. Again, the internal flowfields were established via TAPS, and Al_2O_3 particle trajectories were calculated. Sample plots of such trajectories are shown in Figs. 14 and 15. Additional computer runs were made over the spin rate and axial acceleration spectra, and slag masses were calculated. These results are shown in Fig. 16, as are the corresponding results for the PAM-A and PAM-D motors.

As shown in Fig. 16, the TEM-364-4 and PAM-A motors have negligible amounts of slag as compared with the larger accumulation potentials of the PAM-DII. Even through they may appear to be substantial, the slag quantities predicted for the PAM-DII are far less than one might predict by simply considering the larger geometry and greater propellant quantity. Linear extrapolation or ratioing of such factors as motor dimensions, quantity of propellants, and axial accelerations would result in substantially higher slag quantities if the PAM-D motor is considered as the base of comparison. The reason for this deviation is found in the configuration of the gas flowfield and the direction of the fluid drag forces.

The predictions for the PAM-DII motor were made long before any test data were available. Subsequent to that, the PAM-DII rocket motor was tested at the Arnold Engineering Development Center (AEDC) High-Altitude Test Cell. It was hot fired for full duration at rotation speeds of 30, 50, 70, and 85 rpm. After each firing and cooling, the slag mass was col-

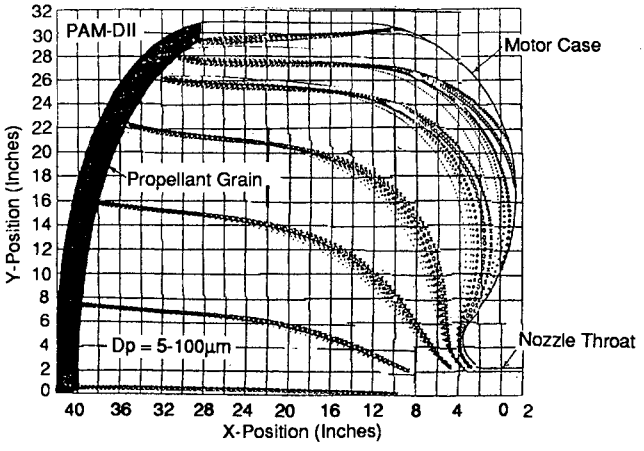

Fig. 15 PAM-D II slag particle trajectories for $\omega = 72$ rpm and $ABX = 210$ ft/s^2.

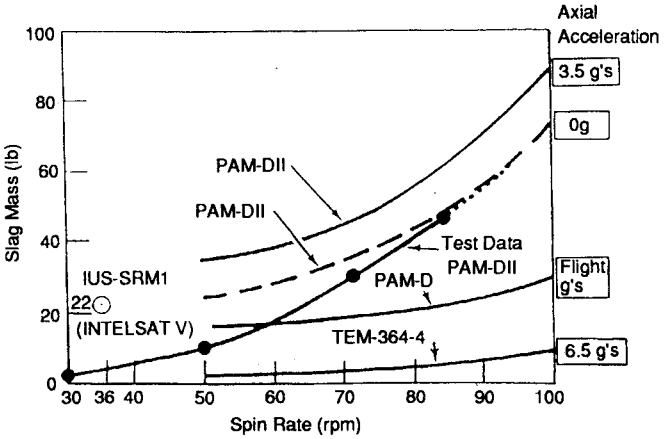

Fig. 16 Slag mass predictions for various motors.

lected, analyzed, and compared with the predictions; results of the comparison are shown in Fig. 16. Very close agreement was obtained at the high spin rates; the predictions for the low spin rates were consistently more than the actual ground test results. The apparent discrepancy is considered acceptable because 1) the analysis models included a closer evaluation of slag particle size and their distribution at high spin rates, and 2) the search was for maximum possible values of slag mass accumulated.

Another consideration in the smaller-than-expected mass accumulations is that the particle-size distributions in the analysis model for most of the Al_2O_3 particles were originally estimated to be in the 4- to 15-μm range. However, experimental results obtained at the AEDC High-Altitude Test Cell indicated a very strong presence of submicron diameter particles.[5] Such a particle-size distribution would result in smaller slag-mass calculations, thus bringing the calculations closer to the actual test data.

Spin and axial acceleration-induced forces tend to drive the particles into the buried nozzle cavity. Fluid drag forces follow the gas streamlines and they may act in a direction that opposes the body forces. Examination of the flowfields near the throat region of the TEM-364-4, PAM-D, and PAM-DII motors reveals that, of the three motors, the PAM-D flowfield is most conducive to slag formation. As shown for each point in Fig. 17, the flow velocity vectors for the TEM-364-4 and the PAM-DII are larger in magnitude and are directed away from the buried nozzle cavity where slag accumulates. The effects of the internal flowfield are fully evaluated in the following section.

Flowfield and Propellant Geometry Effects

The slag particles will move in the direction of the resultant force. The body forces caused by the motor spin and the forward acceleration are of fixed direction. However, the fluid drag acts along the flow streamlines and as such it continuously changes direction. The resultant force is also changing direction because the drag force is governed by the flowfield. Since the combustion gases originate at the propellant burning surface, the geometric configuration of the propellant surface directly affects the flowfield in the motor case.

A motor similar in size to the USAF IUS first-stage motor[6] was selected for this portion of the study. The motor case and the buried nozzle cavity dividing flow streamline were approximated by a series of circular arcs and straight lines and were fed into the computer program. The TAPS potential flow program was used to compute the flowfield again by placing flow sources along the propellant burning surface. The internal flowfield depends on the location of these flow sources and, hence, on the burning surface configuration. A propellant grain corresponding to the last 10 s of burning was considered and placed in different locations, and the flowfield was calculated for each location. The trajectory calculation program was then used to compute and plot the path lines of the Al_2O_3 solid particles originating from the propellant surface. No attempt was made to calculate any specific slag amounts that might be trapped in this large size motor if subjected to simultaneous spin and axial acceleration effects. Instead, the particle trajectory behavior was used to qualitatively describe and assess the effects of the internal flowfield, which is a direct function of the propellant grain configuration.

The data shown in Figs. 18–21 assume a 40-rpm spin rate and a 150-ft/s^2 axial acceleration. The Al_2O_3 particle diameters vary from 5 to 100 μm.

Figure 18 represents the baseline propellant grain configuration near the end of burning (approximately 10 s from burnout). It is seen that all particles originating from the front end of the propellant grain (point A) escape, whereas the larger particles ($D_p > 25$ μm) originating from the aft end of the pro-

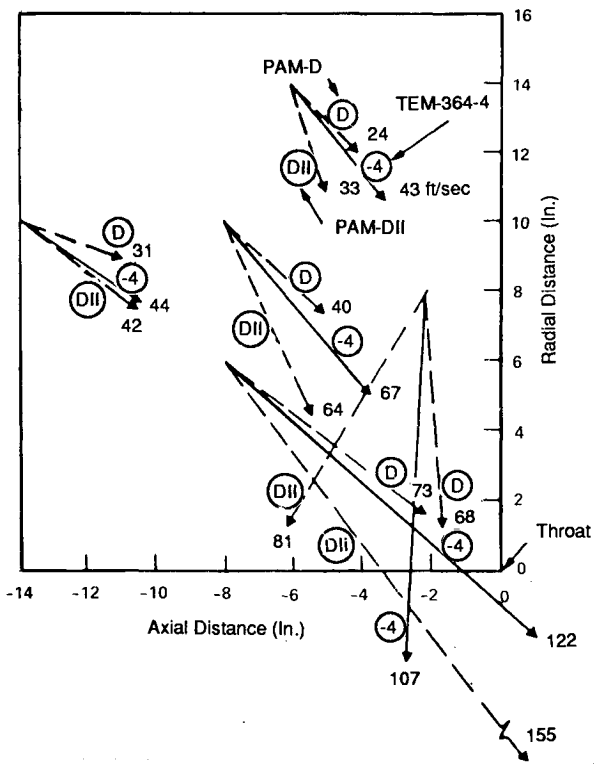

Fig. 17 Velocity flowfield comparison for PAM-D, PAM-DII, and TEM 364-4 motors.

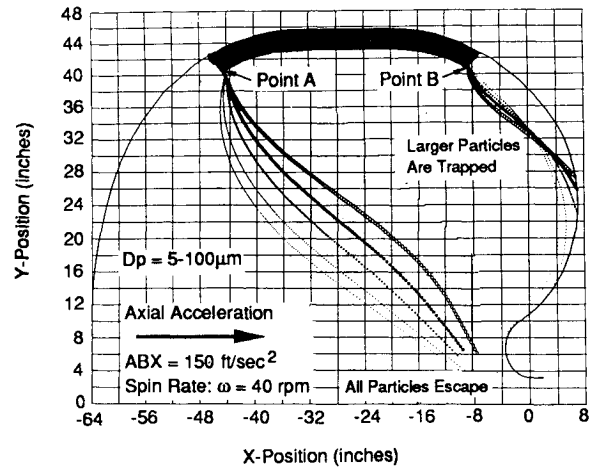

Fig. 18 Large-size rocket motor: baseline configuration.

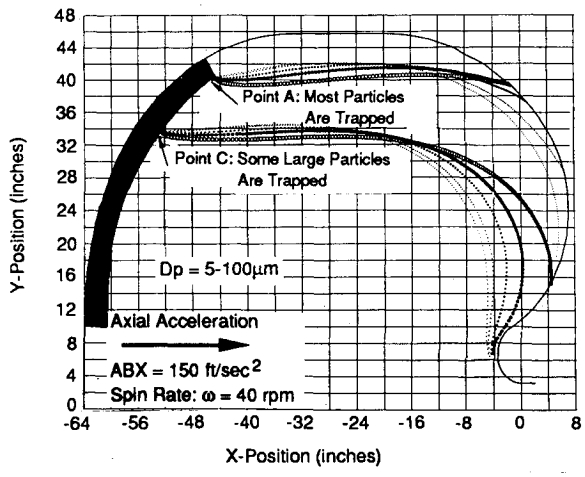

Fig. 19 Large-size rocket motor: head-end burning configuration.

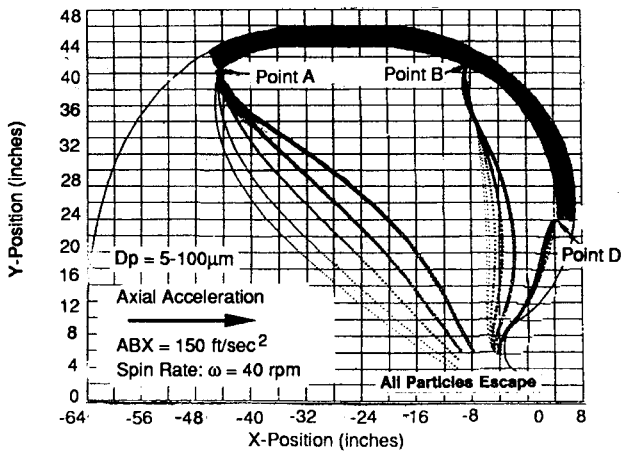

Fig. 20 Large-size rocket motor: buried nozzle cavity burning configuration.

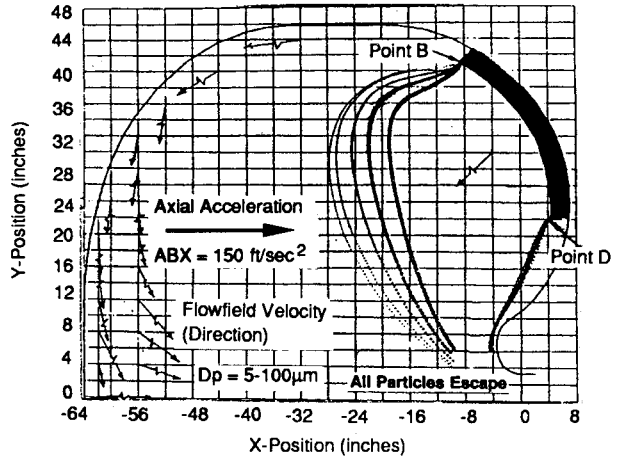

Fig. 21 Large-size rocket motor: aft-end burning configuration.

pellant grain (point B) enter the buried nozzle cavity where they are trapped. Therefore, under these acceleration conditions, one would expect this motor to accumulate a definite amount of slag.

Figure 19 represents the case where the propellant grain is a head-end burner. Here, the flowfield is so different that the drag forces reinforce the body forces in certain areas and cause more particles to be trapped. Point A is the same as in the preceding figure but, whereas previously it did not contribute any slag, here one would expect a substantial contribution from this portion of the grain. Therefore, it can be stated with certainty that this propellant burning configuration would result in substantially more slag accumulation.

The strong effects of the propellant grain configuration during the end of burning are shown in Figs. 20 and 21. The propellant grain has been repositioned to occupy the buried nozzle cavity, which is the slag pocket. As it burns, the propellant grain creates a sweeping flow action that carries all of the particles away from the cavity and out of the nozzle. Thus, this propellant grain configuration will have no slag mass accumulated at all.

Effects of Slag Mass on Performance

The Air Force Astronautics Laboratory (AFAL) Solid Propellant Performance (SPP) computer program[7] was used to evaluate the effects of retained slag mass on the performance of the motor. The amount of the slag was varied from 0 to 100 lb, and its composition was varied from pure unburned aluminum to fully combusted Al_2O_3. The SPP evaluation is based on two kinds of cases.

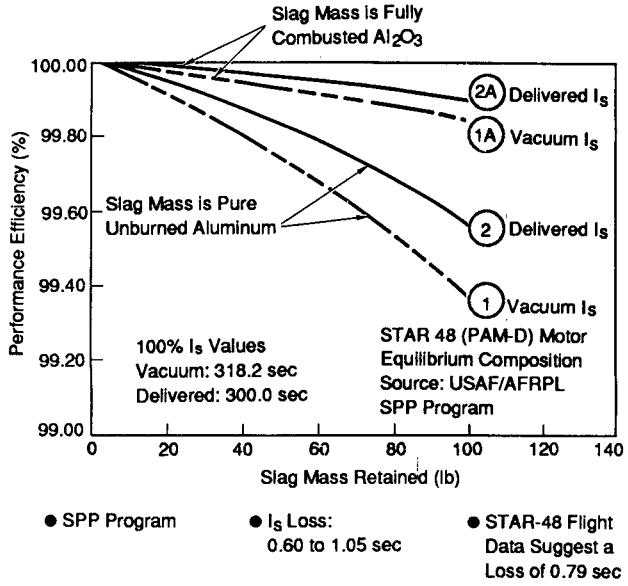

Fig. 22 Effects of slag mass on rocket motor performance.

Case 1: Slag Mass Is Unburned Aluminum

The aluminum content of the propellant is reduced by the mass of the slag, in effect reducing the amount of enthalpy available to the combustion process, in turn resulting in a reduction of the flame temperature. Because aluminum at these temperature levels is liquid, an additional amount of enthalpy corresponding to that required to liquefy the aluminum mass (i.e., the heat of fusion) is subtracted from the combustion process, which further reduces the flame temperature. Both the aluminum content and enthalpy are variables in the SPP program that can be controlled by input.

Case 2: Slag Mass Is Al_2O_3

In this case, the aluminum has combusted and its enthalpy released. The result of the combustion was simulated in the SPP program by removing a corresponding fraction of oxygen from the combustion process actually from the ammonium perchlorate (AP) composition. This simulation, in effect, releases all of the aluminum combustion enthalpy, but because of the lack of available oxygen, some specified amount of Al_2O_3 will not be formed and will therefore not be expelled.[8] The result is identical to the full burning of aluminum to Al_2O_3 except that some of the Al_2O_3 is retained in the motor. A somewhat higher gas exhaust velocity will result because of the loss of inert particles that are a drag in the nozzle flow. One would then anticipate a thrust gain by virtue of the higher exhaust gas velocity, but that gain is offset by a thrust loss due to the lesser ejected mass.

The calculated data for both cases of slag composition followed predictable variations; for example, the performance loss and the variation in flame temperature are greater for the pure aluminum slag than for the Al_2O_3 slag.

Performance results are shown in Fig. 22. Performance losses are not substantial for the two cases studied. Because these cases comprise all of the variations in slag composition, they were considered sufficient.

The first SPP program evaluation was used on the STAR-48 (PAM-D) motor; subsequently, the PAM-DII and the PAM-A displayed similar results.

For a slag mass of 20 lb, the STAR-48 (PAM-D) motor would lose 0.4 s of specific impulse, according to the calculations from the SPP program. Flight data indicate a loss of approximately 0.8 s; this loss contains both the loss caused by the mass not expelled out the nozzle and the loss caused by this mass having to be accelerated. The conclusion, therefore, is that the performance loss calculations presented here correlate

very well with the flight data. Based on the results obtained from the SPP program, no other performance evaluations were considered necessary.

Additional details and information on these points may be found in Refs. 9 and 10.

Conclusions

A method has been presented for calculating the slag mass accumulation in spin-stabilized solid rocket motors. The method has been successfully applied to a variety of specific cases and invariably the predictions have correlated well with ground test and flight-telemetered data. One important conclusion is the effect of the propellant grain configuration and how if it is shaped to burn in the potential slag-accumulating cavities near the burnout, then the slag mass accumulation is completely eliminated. Furthermore, it has been shown that the performance loss caused by the slag mass trapped in the motor case is small.

Acknowledgment

This work was done under the McDonnell Douglas Corporation Independent Research and Development Program.

References

[1]Boraas, S., "Modeling Slag Deposition in the Space Shuttle Solid Rocket Motor," *Journal of Spacecraft and Rockets,* Vol. 21, No. 1, 1984, pp. 47–54.

[2]Gentry, A. E., and Wazzan, A. R., "The Transition Analysis Program System," Vols. I and II, McDonnell Douglas Astronautics Company, MDC J7255, June 1976.

[3]Hess, J. L., and Smith, A. M. O., "Calculation of Potential Flow About Arbitrary Bodies," *Progress in Aeronautical Sciences,* Vol. 8, edited by D. Küchemann, Pergamon, New York, 1966.

[4]Haloulakos, V. E., and Davis, J. C., "Slag Formation Analysis," Chemical Propulsion Information Agency, Applied Physics Lab., Laurel, MD, CPIA Publication No. 370, Vol. II, Feb. 1983, pp. 39–47.

[5]Girata, P. T., Jr., and McGregor, W. K., "Particle Sampling of Solid Rocket Motor Exhausts in High-Altitude Test Cells," *Progress in Astronautics and Aeronautics: Space Contamination: Sources and Preventions,* Vol. 91, edited by J. A. Roux and T. D. McCay, AIAA, New York, 1984, pp. 293–309.

[6]Chase, Charles A., "IUS Solid Rocket Motors Overview," Chemical Propulsion Information Agency, Applied Physics Lab., Laurel, MD, CPIA Publication No. 370, Vol. I, Feb. 1983, p. 101.

[7]Nickerson, G. R., and Coats, D. E., "A Computer Program for the Prediction of Solid Rocket Motor Performance," Vols. I, II, and III, Air Force Rocket Propulsion Lab., Edwards AFB, CA, AFRPL-TR-80-34, April 1981.

[8]Special conference with Nickerson, G. R., and Coats, D. E., Solid Propellant Performance Program (Ref. 7).

[9]Haloulakos, V. E., "Rocket Motor Slag Formation; Effects of Internal Flow Field and Propellant Grain Configuration," Chemical Propulsion Information Agency, Applied Physics Lab., Laurel, MD, CPIA Publication No. 425, Vol. I, April 1985, p. 345.

[10]Haloulakos, V. E., "Slag Mass and Two-Phase Nozzle Flow Asymmetry Effects on Rocket Motor Performance," Chemical Propulsion Information Agency, Applied Physics Lab., Laurel, MD, CPIA Publication No. 455, Vol. I, Aug. 1986, p. 489.